



HAL
open science

Measurement of near-field thermal radiation between multilayered metamaterials

Sen Zhang, Yongdi Dang, Xinran Li, Naeem Iqbal, Yi Jin, Pankaj Choudhury,
Mauro Antezza, Jianbin Xu, Yungui Ma

► **To cite this version:**

Sen Zhang, Yongdi Dang, Xinran Li, Naeem Iqbal, Yi Jin, et al.. Measurement of near-field thermal radiation between multilayered metamaterials. *Physical Review Applied*, 2024, 21 (2), pp.024054. 10.1103/PhysRevApplied.21.024054 . hal-04608582

HAL Id: hal-04608582

<https://hal.science/hal-04608582v1>

Submitted on 11 Jun 2024

HAL is a multi-disciplinary open access archive for the deposit and dissemination of scientific research documents, whether they are published or not. The documents may come from teaching and research institutions in France or abroad, or from public or private research centers.

L'archive ouverte pluridisciplinaire **HAL**, est destinée au dépôt et à la diffusion de documents scientifiques de niveau recherche, publiés ou non, émanant des établissements d'enseignement et de recherche français ou étrangers, des laboratoires publics ou privés.

Measurement of near-field thermal radiation between multilayered metamaterials


Sen Zhang¹, Yongdi Dang¹, Xinran Li¹, Naeem Iqbal¹, Yi Jin¹, Pankaj K. Choudhury¹,
Mauro Antezza^{2,3}, Jianbin Xu⁴, and Yungui Ma^{1,*}

¹*State Key Lab of Modern Optical Instrumentation, Centre for Optical and Electromagnetic Research, College of Optical Science and Engineering, International Research Center for Advanced Photonics, Zhejiang University, Hangzhou, China*

²*Laboratoire Charles Coulomb (L2C), UMR 5221 CNRS-Université de Montpellier, F-34095 Montpellier, France*

³*Institut Universitaire de France, 1 rue Descartes, F-75231 Paris Cedex 05, France*

⁴*Department of Electrical and Electronic Engineering, The University of Hong Kong, Pokfulam Road, Hong Kong, China*

 (Received 22 October 2023; revised 29 December 2023; accepted 5 February 2024; published 28 February 2024)

The near-field radiative heat transfer (NFRHT) between one-dimensional metamaterials comprised of phonon dielectric multilayers was investigated experimentally. Large-size ($1 \times 1 \text{ cm}^2$) near-field samples were fabricated using SiC, SiO₂, and Ge layers at a certain gap distance, and the effects of layer-stacking order and phonon-resonance quality on NFRHT were examined. The measured results show good agreement with the theoretical results obtained by employing the transmission-matrix method. Super-Planckian thermal radiation was observed between emitters and receivers with identical structures. The failure of effective-medium theory (EMT) at predicting the near-field heat flux has been evidenced by measurements, particularly in the presence of bounded surface modes, such as the epsilon-near-zero mode. Additionally, analyses have shown that, in specific scenarios, the EMT can offer reasonable physical insights into the underlying coupling process from the perspective of homogenized media. Furthermore, the conditions for applying the EMT in the near-field regime were also touched upon.

DOI: [10.1103/PhysRevApplied.21.024054](https://doi.org/10.1103/PhysRevApplied.21.024054)

I. INTRODUCTION

Radiative heat emission is a fundamental physical process that occurs when charged particles or quasiparticles in matter vibrate randomly due to thermal agitation, which has widespread technological applications. Enhancing the radiation strength has been a fundamental focus of scientific research. In the far-field regime, the upper limit of radiation strength is determined by the blackbody. However, in the near-field regime, where the distance between the emitter and receiver is much smaller than the thermal wavelength, evanescent waves with a high localized density of states (LDOS) can participate in heat transfer by tunneling through the gaps [1]. This effect could significantly enhance the spontaneous radiation power, exceeding the blackbody limit by several orders. A study of this so-called super-Planckian thermal radiation was first reported for heat exchange between semi-infinite planar surfaces using fluctuational electrodynamics (FE) [2], and later generalized to arbitrary geometries and materials [3–8]. The near-field radiative heat transfer (NFRHT) can be substantially intensified when bounded surface

modes exist, such as the surface plasmon polaritons [9–13], surface phonon polaritons (SPhPs) [14,15], and hybrid polaritons [13,16–18]. These localized field effects can be found in natural materials within infrared bands.

Alternatively, metamaterial-inspired artificial structures have received increased attention for their ability to control thermal radiation by offering parametric freedoms to produce versatile electromagnetic properties in various frequency bands [19–23], aimed to operate at different temperatures. However, relevant experiments on artificial structures for NFRHT are rare [13,24–28] because the fabrication of high-quality infrared metamaterials with superflat surfaces, along with the required size, is challenging. Also, it is rather difficult to calculate the radiation of artificial structures, especially in the near-field regime [29–32]. Homogenization algorithms, such as effective-medium theory (EMT), can simplify the analysis of metamaterials with unit cells much smaller than the wavelength scale or the separation gaps [25,33,34]. Generally, EMT can provide only a qualitative explanation for light-matter interactions when the evanescent fields are dominant. The exact solution may be obtained by advanced mathematical tools, such as the rigorous coupled-wave analysis, but it requires substantial computation time and resource

*yungui@zju.edu.cn

requirements [32,35,36]. However, alternative methods have been recently developed to tackle this complexity [37]. Low computation efficiency and experimental challenges hinder the application of complex artificial electromagnetic structures in near-field thermal radiation.

Thin-film-based multilayer one-dimensional (1D) artificial structures have been widely explored with exotic features for various applications, such as thermophotovoltaics [38,39], thermal management [20,40–44], thermal imaging [45], and Casimir forces [46–48]. In the near-field regime, multilayers possess some advantages, such as the stacking configuration can be freely employed to engineer hyperbolic band diagrams [49], and more importantly, their thermal emission or absorption in the semi-infinite framework can be analyzed using the transfer-matrix method (TMM). This analytical approach enables the introduction of 1D structures into near-field thermal radiation. Lee and co-workers experimentally examined such potential using metal-dielectric multilayers based on a complicated microelectromechanical measurement system [13]. They demonstrated that the multilayer generated a much higher near-field heat flux than the individual components. Additional experimental studies are necessary to uncover the underlying physics and the potential of multilayer structures for NFRHT. It is also essential to investigate them for samples of macroscopic sizes [50,51].

Here, we fabricate centimeter-sized multilayers composed of dielectric thin films featuring different phonon resonances and explore NFRHT between them. We experimentally investigate the effect of layer composition and stacking order, and the results show good agreement with the theoretically obtained ones using the TMM route. When the emitter and receiver have identical structures, super-Planckian thermal radiation is observed due to different near-field coupling channels arising from the phonon resonances and frustrated total internal reflections. Theoretical analyses indicate that, although it generally fails to predict the near-field heat flux, the use of EMT can still give reasonable physical insights into the near-field coupling from band diagrams. The reliability of EMT in the near-field regime is further discussed in relation to the ratio of the gap distance to the unit-cell period in multilayer metamaterials. These results are instrumental for understanding the role of metamaterials in the near-field regime and may boost their applications in the thriving field of near-field thermal management.

II. SAMPLE CHARACTERIZATION

Figure 1(a) provides a schematic illustration of the dielectric multilayer structure comprised of the unit cells of SiC/Ge and SiO₂/Ge films. We chose SiC and SiO₂ due to their distinct phonon-resonance characteristics; Ge is a lossless dielectric spacer with a constant permittivity in the

relevant frequency bands. We employed magnetron sputtering to deposit alternating SiC/Ge and SiO₂/Ge layers on the substrate coated with a metal film in four stacking orders: sample I, [SiC/Ge]_n/metal/substrate; sample II, [Ge/SiC]_n/metal/substrate; sample III, [SiO₂/Ge]_n/metal/substrate; and sample IV, [Ge/SiO₂]_n/metal/substrate. The power of the radio-frequency source was set to 60 W for SiC and Ge and 100 W for SiO₂, while the gas pressure was 5 mTorr and controlled by an argon valve. The deposition rates for SiC, SiO₂, and Ge are 1.35, 1.42, and 5.45 nm/min, respectively. For sample I (II), the outermost layer in contact with the vacuum is SiC (Ge), whereas for sample III (IV), it is SiO₂(Ge). Each sample consists of three unit cells ($n=3$) with a period of 110 nm and a total thickness of around 330 nm. The samples were grown over a 500- μ m-thick silicon substrate presputtered with a 100-nm-thick Al film. We selected silicon substrates with acceptable bending conditions. The multilayer samples have a surface size of 1×1 cm² with an average roughness of about 1.6 nm. Details on bending and surface-roughness morphology can be found in the Appendix. During the experiment, we assembled four samples in different combinations, as described below.

Figure 1(b) exhibits the measurement setup placed in a high-vacuum chamber with a pressure of $<10^{-4}$ Pa. The upper part of the setup, referred to as the emitter side, consists of the load, heater, and copper heat spreader (with an embedded thermistor, ± 1 K accuracy). The lower receiver part comprises the multilayer sample, copper heat spreader (also with an embedded thermistor, ± 1 K accuracy), heat-flux sensor (HFS; HS-10 Captec, France, accuracy $\sim 3\%$ and sensitivity $\sim 0.12 \mu\text{V W}^{-1} \text{m}^2$), and a temperature electric controller (TEC). To minimize the contact thermal resistances, we assembled the components in each part using thermal conductive glue. We conducted separate experiments to evaluate the internal conductive thermal resistances of the emitter (receiver), from which we could derive the real temperature, T_e (T_r), of the emitter (receiver); the calibration details can be found in Appendix. In experiments, T_r was stabilized at around 295 K using TEC. The HFS was read by the source meter (Keithley 2450, 6.5-bit accuracy). The emitter and receiver were separated by four cylindrical photoresist nanopillars (SU8, thermal conductivity $\kappa = 0.3 \text{ W m}^{-1} \text{K}^{-1}$) having heights and diameters of (270 ± 6) nm and 20 μ m, respectively, which were fabricated using UV lithography (MA6/BA6, SUSS MicroTec, Germany) at the four corners of the chip. The photoresist fabrication details can be found in our previous work [52]. Moreover, a 10-g load was placed on the emitter to ensure an appropriate pressure and achieve surface uniformity. The gap distance is thus decided by the height of the nanopillars, as examined in our previous work [53].

Figure 1(b) also shows the equivalent thermal circuit of our measurement, with R_{rad} (R_{con}) representing the

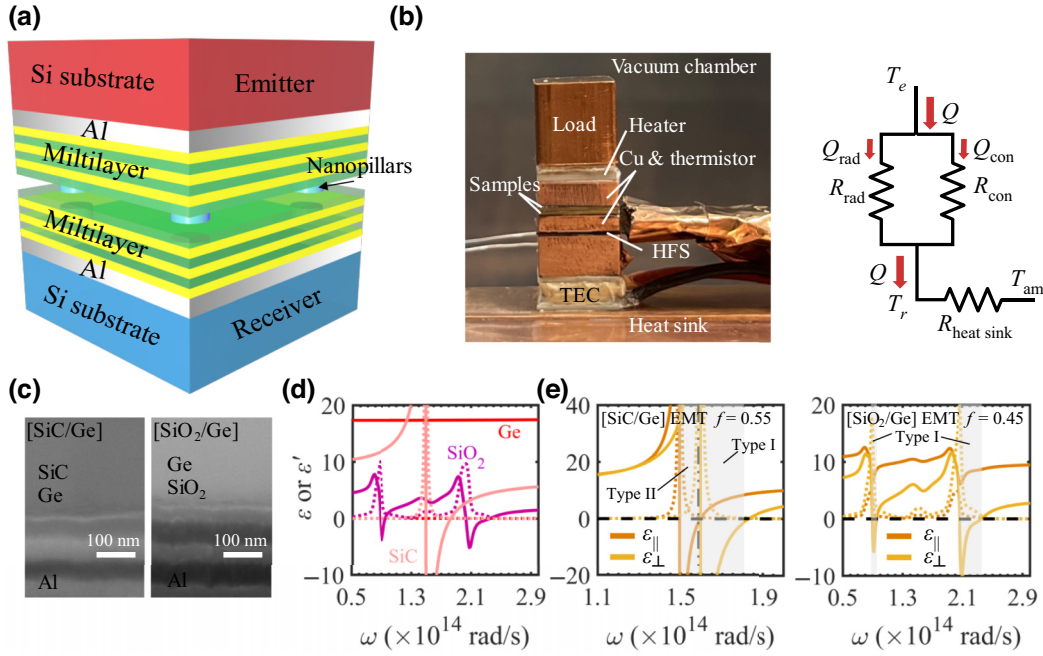


FIG. 1. (a) Schematic of the dielectric multilayer structures. Emitter and receiver are separated by photoresist nanopillars with a gap distance of d . (b) NFRHT measurement setup. Two embedded thermistors (not shown here) are used to measure local temperatures of heat spreaders. Right figure is the thermal resistance network of the thermal pathway. T_e , T_r , and T_{am} represent the temperature of emitter, receiver, and ambient chamber, respectively. R_{rad} , R_{con} , and R_{rad} represent the effective thermal resistance of near-field radiation, conduction through the pillars, and conduction through the heat sink, respectively. (c) SEM images of the cross section of the fabricated multilayer samples. Effective permittivity spectra for (d) bulk materials and (e) [SiC/Ge] and [SiO₂/Ge] multilayer samples. $\epsilon^{(i)}$ corresponds to the real (imaginary) part of the dielectric constant, while the parallel (perpendicular) portion to the surface plane is denoted as $\epsilon_{||(\perp)}$. Filling ratios, f , of SiC or SiO₂ are also provided based on the actual thicknesses. Hyperbolic bands are marked by the shaded regions in (e).

thermal resistance of the radiation (conduction through nanopillars) channel. The quantity Q denotes the total heat flux exchanged between the emitter and receiver, and Q_{rad} (Q_{con}) describes the part contributed to the radiation (conduction) channel. As such,

$$Q = Q_{rad} + Q_{con}. \quad (1)$$

The near-field radiation heat flux can be analytically calculated from the FE as [25]

$$Q_{rad} = \frac{1}{8\pi^3} \int_0^\infty [\Theta(\omega, T_e) - \Theta(\omega, T_r)] H(\omega) d\omega, \quad (2)$$

where $\Theta(\omega, T) = \hbar\omega / e^{\hbar\omega/k_B T} - 1$ is the mean energy of the Planckian oscillator and $H(\omega) = 2\pi \int_0^\infty (\tau_s + \tau_p) k_{||} dk_{||}$ is the spectral heat-transfer coefficient; $\tau_{s,p}$ is the energy-transmission coefficient for the s - or p -polarized waves. For a multilayer structure, we use the TMM to acquire the rigorous energy-transmission coefficient [54] and EMT for the homogenization results [55]. The heat flux via conduction, Q_{con} , is

$$Q_{con} = \kappa N S_{NP} \Delta T / d, \quad (3)$$

where $\Delta T = T_e - T_r$, N is the number of nanopillars, and S_{NP} is the top surface area of the nanopillars. Q_{con} needs to be converted into the power-density unit when applying Eq. (1).

Figure 1(c) provides the cross-section view of samples obtained by scanning electron microscopy (SEM; Zeiss, Germany). High-quality films with clear multilayer interfaces are fabricated. The thicknesses of the SiC/Ge and SiO₂/Ge multilayers were precisely controlled to be identical for different stacking orders by maintaining deposition conditions. Overall, the multilayer thicknesses are [SiC(60 nm)/Ge(48 nm)]₃ and [SiO₂(50 nm)/Ge(62 nm)]₃, while the thickness nonuniformity is discussed in the Appendix. It should be noted that samples with the same compositions and thickness ratios but different stacking orders demonstrate identical uniaxial parameters in terms of the EMT approximation. In the quasistatic limit, we initially employ EMT to analyze the physical properties of multilayers, considering the parallel ($||$) and perpendicular (\perp) components of dielectric functions by [56]

$$\epsilon_{||} = \frac{\epsilon_1 d_1 + \epsilon_2 d_2}{d_1 + d_2}, \quad (4)$$

$$\varepsilon_{\perp} = \frac{\varepsilon_1 \varepsilon_2 (d_1 + d_2)}{\varepsilon_1 d_2 + \varepsilon_2 d_1}, \quad (5)$$

where ε_i and d_i (with $i = 1, 2$) represent the dielectric constants and thicknesses of SiC (SiO₂) and Ge, respectively. Later, we show that the EMT approximation could qualitatively explain near-field coupling, although heat flux may exhibit large deviations in amplitude at small gaps.

The dielectric functions of SiC and SiO₂ are $\varepsilon_{\text{SiC}} = \varepsilon_{\infty}(\omega^2 - \omega_{\text{LO}}^2 + i\omega\gamma)/(\omega^2 - \omega_{\text{TO}}^2 + i\omega\gamma)$ and $\varepsilon_{\text{SiO}_2} = \varepsilon_{\infty} + \sum_j [g_{c_j}^{\text{kg}}(\eta) + ig_{e_j}(\eta)]$, respectively, and details can be found in the literature [57,58]. Figure 1(d) depicts the dielectric constants. SiC and SiO₂ are polar materials with strong phonon resonances in the infrared bands. Usually, SPhPs give rise to strong surface LDOS and significantly enhance NFRHT. In this region, Ge simply behaves as a lossless medium with a permittivity of approximately 16. To meet the long-wavelength approximation condition, the unit period, p ($=d_1 + d_2$), of multilayers should be far smaller than the radiation wavelength and gap distance. Under these conditions, the multilayer samples can be approximated with a hyperbolic elliptic dispersion by [56]

$$\frac{k_{\parallel}^2}{\varepsilon_{\perp}} + \frac{k_{\perp}^2}{\varepsilon_{\parallel}} = \frac{\omega^2}{c^2}, \quad (6)$$

where k_{\parallel} (k_{\perp}) is the in-plane (out-of-plane) wave vector and c is the speed of light in a vacuum. Basically, the hyperbolic dispersion relation can be satisfied with type-I ($\varepsilon_{\parallel} > 0$, $\varepsilon_{\perp} < 0$) and type-II ($\varepsilon_{\parallel} < 0$, $\varepsilon_{\perp} > 0$) configurations.

Multilayer designs offer parametric freedoms in optimizing optical properties to precisely match the spontaneous thermal emission spectrum of radiators. In the quasistatic regime, the condition $\varepsilon_{\perp} \varepsilon_{\parallel} = -1$ gives rise to a near-field blackbody made of hyperbolic materials [59–61]. However, achieving this condition is difficult due to

material imperfections. Figure 1(e) shows the in-plane and out-of-plane complex permittivity spectra of the homogenized multilayers at realistic thicknesses. For the SiC/Ge composite, there are two types of hyperbolic subbands, namely, type II $\in [1.50 \times 10^{14} \text{ rad/s}, 1.59 \times 10^{14} \text{ rad/s}]$ and type I $\in [1.59 \times 10^{14} \text{ rad/s}, 1.82 \times 10^{14} \text{ rad/s}]$, and the SiO₂/Ge composite exhibits two type-I hyperbolic bands, that is, $[0.89 \times 10^{14} \text{ rad/s}, 0.95 \times 10^{14} \text{ rad/s}]$ and $[2.06 \times 10^{14} \text{ rad/s}, 2.35 \times 10^{14} \text{ rad/s}]$. Based on Eq. (6), when the loss is negligible, k_{\parallel} can take very large values ($\gg k_0 = \omega/c$) for the type-I hyperbolic band, keeping k_z dominantly a real number, which is the key feature of hyperbolic media. As for the type-II band, k_z is only real when $k_{\parallel} > \sqrt{\varepsilon_{\perp}} k_0$. At our operating temperature range (300–350 K), the hyperbolic modes (HMs) dominate the near-field thermal radiation, in particular for bands where $\varepsilon_{\perp} \varepsilon_{\parallel} = -1$ is approximately satisfied [61]. The peaks in the permittivity spectra manifest phonon resonances of the dielectric constituents.

III. MEASUREMENT RESULTS

Figure 2 shows the measured and calculated near-field heat flux between different combinations of SiC/Ge and [SiO₂/Ge] multilayers as a function of temperature bias, $\Delta T = T_e - T_r$. Results were obtained at the same gap distance of 270 nm. The experimental data were collected through five measurement replicates. The Q error bars (too small to be distinguished) are obtained from the accuracy of the heat-flux sensor (3%). The temperature uncertainty is ± 1 K and is not shown in the figure. The theoretical results are calculated in terms of the uncertainties in chip bending, roughness, height of the nanopillars, and multilayer thickness, as discussed in the Appendix. To explore the significance of the SPhPs-mode coupling effect in multilayers, experiments were conducted using configurations I-I, I-II, III-III, and III-IV. In scenarios II-II

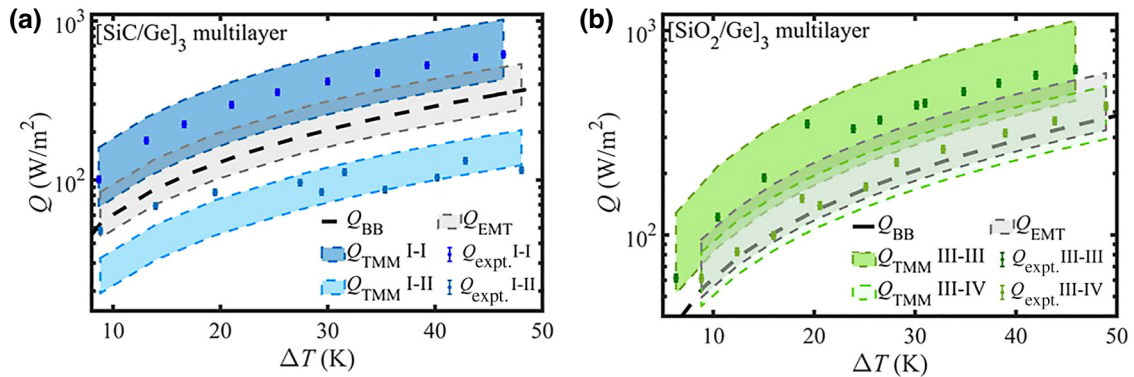


FIG. 2. Comparison of NFRHT between (a) I-I and I-II and (b) III-III and III-IV combinations, with $\Delta T = T_e - T_r$. TMM and EMT theoretical predictions (Q_{TMM} and Q_{EMT}) are plotted with shaded areas based on uncertainty analyses. Blackbody limit, Q_{BB} (black dashed line), is also provided. Experimental results, $Q_{\text{expt.}}$, are plotted as dot symbols with error bars ($\pm 3\%$), which are relatively small and indistinguishable in the figure.

or IV-IV, the absence of a surface mode at the vacuum-Ge interface indicates that these configurations are not suitable for the investigation. Good agreement between the measured ($Q_{\text{expt.}}$) and theoretical (Q_{TMM}) results validate our experimental assumption on the conductive contribution through nanopillars. We also show the blackbody limit, Q_{BB} , for comparison. The measured results for combinations of samples I-I and III-III are 1.65 and 1.77 times, respectively, of the blackbody-radiation limit, thereby indicating the positive role of SPhPs in NFRHT. In Fig. 2(a), we see the achieved modulation depth of 5.40 for heat flux for combinations of samples I-I when compared with samples I-II. Measurements indicate the layer-stacking order in the emitter and receiver to be prominent with respect to heat flux in the near-field scenario. It seems reasonable, as the surface-mode coupling is weak with the existence of a lossless-Ge outermost layer. In addition, the heat flux, Q_{EMT} , predicted by EMT significantly deviates from experimental data for combinations of samples I-I and I-II. Measurements show that the outermost layer is critical when deciding the overall near-field heat flux, thus challenging the applicability of EMT. In Fig. 2(b), we demonstrate the NFRHT behaviors of $[\text{SiO}_2/\text{Ge}]$ multilayers for comparison. The heat-flux discrepancy observed between the two combinations of samples III-III and III-IV almost disappears,

corresponding to a small flux-modulation depth of 1.67. EMT gives comparatively smaller prediction errors for combinations of samples III-IV and III-III. Furthermore, the proportions of near-field radiation, $Q_{\text{expt.}}$, to the total heat flux ($Q_{\text{expt.}} + Q_{\text{con}}$) at the data point with maximum temperature bias are 78%, 40%, 79%, and 71% for samples I-I, I-II, III-III, and III-IV, respectively.

IV. DISCUSSION

To further understand the underlying physics related to NFRHT between multilayer metamaterials, we obtained the p -polarized transmission coefficient, τ_p , as a function of normalized wave vector, k_{\parallel}/k_0 , and angular frequency, ω , using both the TMM and EMT. As Fig. 3 illustrates, basically, the dielectric multilayers support two distinct types of resonance modes: one is frustrated modes (FMs), where the waves are propagating inside the material but evanescent under vacuum, and the other is SPhP modes, with waves being evanescent at both sides. In Fig. 3(a), for the combination of samples I-I (identical SiC/Ge multilayers), the TMM approach reveals two prominent SPhP bands originating from the near-field coupling of resonance modes between nearby SiC layers at $1.5\text{--}1.9 \times 10^{14}$ rad/s [57]. These strongly coupled modes

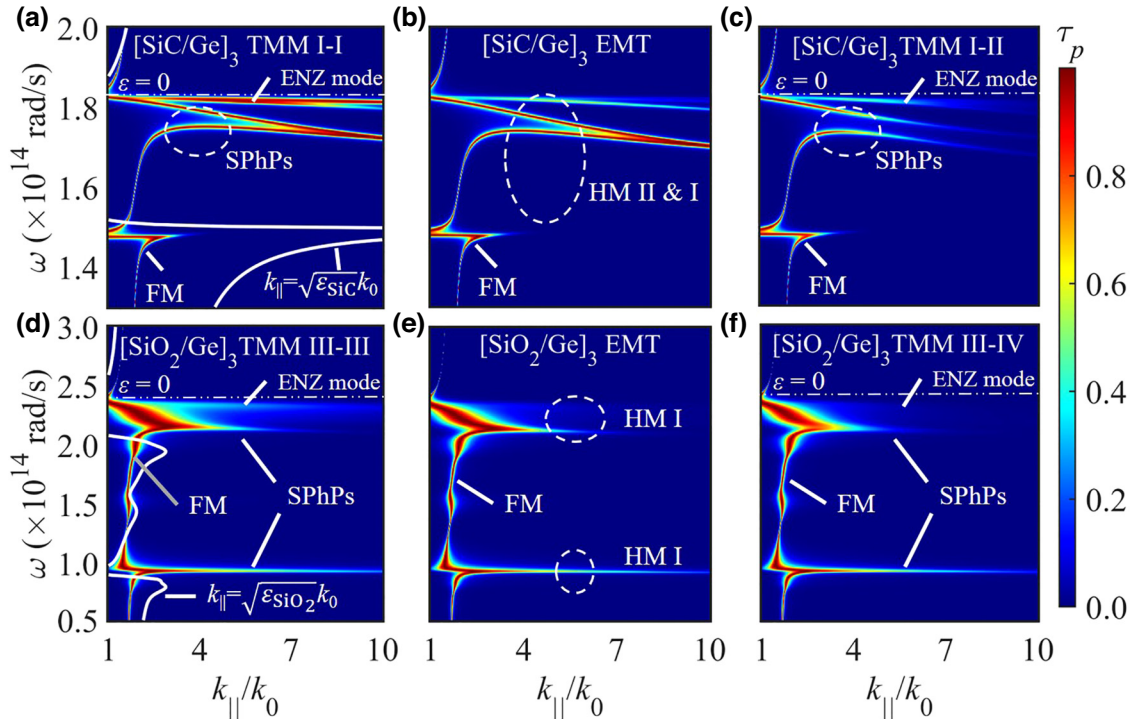


FIG. 3. p -Polarized transmission coefficients, τ_p , of SiC/Ge and $[\text{SiO}_2/\text{Ge}]$ multilayers in different layer-stacking orders for emitter and receiver calculated by the EMT and TMM approaches. Calculations are conducted at 270-nm gap distance. (a),(d) and (c),(f) correspond to TMM calculations, where the light cone for SiC and SiO₂ are depicted as white lines. EMT results are plotted in (b),(e) for comparison.

can significantly enhance NFRHT by transferring evanescent waves with large k_{\parallel} . Similarly, enhanced transmission due to the SPhP-resonance coupling for the combination of samples III-III (identical $[\text{SiO}_2/\text{Ge}]$ multilayers) is observed at about 0.9×10^{14} and 2.1×10^{14} rad/s, as shown in Fig. 3(d). Compared with SiC, the larger dielectric loss of SiO_2 weakens the near-field coupling, as indicated by the narrower distribution range for k_{\parallel} and broader transmission peaks. In addition, enhanced photon transmission due to the FM contribution is observed at about 1.47×10^{14} rad/s in Fig. 3(a) and about 2.0×10^{14} rad/s in Fig. 3(d), where multilayers exhibit a high-index lossy material. However, when compared with the bounded surface modes, the contribution ratio of FM is relatively small, as it has a lower cutoff for the in-plane wave vector, i.e., $k_{\parallel} < \sqrt{\epsilon_i} k_0$ (marked with white lines in Fig. 3). Besides the FM and SPhP modes, one flat band profiled by the white dashed lines also appears in Figs. 3(a) and 3(d) at about 1.8×10^{14} and 2.3×10^{14} rad/s, respectively. Close inspection indicates that this band could be attributed to the classic epsilon-near-zero (ENZ) mode, where $\epsilon = 0$ for SiC or SiO_2 [62,63], excited at the interface of vacuum-SiC or vacuum- SiO_2 of a thin slab. The ENZ mode related to the uppermost dielectric layer offers another channel for the tunneling of thermal evanescent waves.

Figures 3(b) and 3(e) plot the transmission coefficients calculated by homogenizing the SiC/Ge and $[\text{SiO}_2/\text{Ge}]$ multilayers into uniaxial anisotropic effective media. Interestingly, the EMT gives rise to very similar dispersion characteristics, with those shown in Figs. 3(a) and 3(d) obtained by rigorous theory. In addition to the FM pattern, hyperbolic diagrams exist; these are calculated using the effective-medium approximation parameters described in Fig. 1(e). There are two different types of hyperbolic bands for the SiC/Ge medium and one type of hyperbolic band for the SiO_2/Ge medium. Coincidentally, the different-ordered waveguide modes supported by the HM thin film induce similar transmission features in the frequency and wave-vector space to those considering interlayer-field-coupling TMM results. From the comparison, it is reasonable to conclude that, although it fails to give a quantitative explanation of the near-field heat flux, the EMT analysis in certain cases can still be meaningful to understand the underlying physical process from the perspective of homogenized media.

In Figs. 3(c) and 3(f), the emitter and receiver are assembled with different layer-stacking orders. The notable difference is that the two SPhP curves in Fig. 3(a) do not converge at large k_{\parallel} . Close inspection of the dispersion pattern indicates that this difference is caused by the momentum mismatch between SPhP modes excited at the vacuum-SiC and Ge-SiC interfaces when the multilayer's ingredients in the emitter and receiver are of asymmetrical distribution. It is similar to previous results observed between two monolayers of graphene having different

Fermi levels [64]. In a symmetric configuration, these two SPhP modes become identical at very large wave vectors and their bands merge when the decay length of the surface mode becomes comparable to the gap distance. This fine feature cannot be predicted by EMT, as it does not consider the stacking order. For the $[\text{SiO}_2/\text{Ge}]$ multilayer, comparing Figs. 3(d) and 3(f), we see that the transmission patterns show little dependence on the layer-stacking order for those related to the SPhP modes, primarily due to the relatively high damping rate of SiO_2 . But in this case, the ENZ mode nearly disappears in Fig. 3(f). It is reasonable, as the ENZ mode for the outermost SiO_2 layer is sensitive to the dielectric background. Without this mode, the combination of samples III-IV has a very similar overall transmission pattern [Fig. 3(f)] to that [Fig. 3(e)] predicted by EMT, in agreement with their similar heat fluxes plotted in Fig. 2(b).

Figure 4 shows the obtained spectral heat-transfer coefficient, $H(\omega)$, normalized to that of the blackbody, $H_{\text{BB}}(\omega)$ ($=2\pi k_0^2$), for the SiC/Ge and $[\text{SiO}_2/\text{Ge}]$ multilayers. We also provide the results for bulky SiC and SiO_2 for comparison. In Fig. 4(a), the first peak appears at 1.49×10^{14} rad/s, which stems from the FM contributions of multilayers. In this region, the behaviors of bulk SiC, EMT, and TMM results for combinations of samples I-I and I-II are nearly the same. In contrast, the second peak appearing around 1.75 – 1.85×10^{14} rad/s shows large deviations. For the $[\text{SiO}_2/\text{Ge}]$ multilayer [Fig. 4(b)], the first and second peaks emerge, respectively, at 0.93×10^{14} and 2.10 – 2.40×10^{14} rad/s, corresponding to the two phonon resonances of SiO_2 . For the results on identical combinations (I-I and III-III), calculated by the TMM, significant enhancement is attributed to the ENZ modes of the outermost SiC and SiO_2 layers. The ENZ peaks

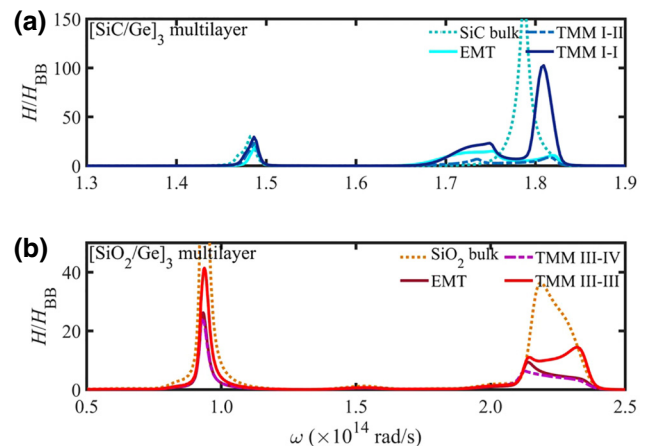


FIG. 4. Near-field spectral heat flux for different combinations of (a) SiC/Ge and (b) $[\text{SiO}_2/\text{Ge}]$ multilayer samples. Spectral heat flux is normalized to that of the blackbody with H/H_{BB} . Results of bulk SiC and SiO_2 are also provided for comparison.

appear at 1.82×10^{14} and 2.33×10^{14} rad/s for SiC/Ge and [SiO₂/Ge], respectively; these values agree well with the dispersion relation analyzed in Fig. 3. The EMT approximation cannot predict the ENZ band, as it is purely a localized mode originating from the outermost phonon SiC or SiO₂ layer. This may be the major reason for the discrepancy in heat flux calculated by the TMM and EMT. Besides, compared with the bulk media, the shift of the SPhP-resonance frequency also indicates the evolution from bulk SPhPs towards ENZ modes in thin films.

Next, we theoretically explore the condition of applying EMT to predict the NFRHT behaviors between dielectric multilayers. We obtain the results of EMT compared to TMM [$\log_{10}(h_{\text{EMT}}/h_{\text{TMM}})$] based on the same triple-period [SiC/Ge]₃ and [SiO₂/Ge]₃ multilayers, as Fig. 1(a) illustrates. The quantities h_{EMT} and h_{TMM} are the heat-transfer coefficients obtained by taking partial derivatives of temperature in Eq. (2) at 300 K. Figure 5 numerically plots the flux deviations via the gap distance (d changing from 10 nm to 1 μm) and unit-cell period (p changing from 10 to 450 nm). The thickness of each layer is set to $0.5p$. The contour lines comprehensively evaluate the prediction errors of EMT across the entire parametric space. In general, EMT tends to overestimate NFRHT between multilayers, where the outermost layer does not support surface

modes [Figs. 5(a) and 5(c)]. On the contrary, EMT underestimates NFRHT between multilayers, with an outermost layer that supports surface modes [Figs. 5(b) and 5(d)]. The effect of this deviation has positive or negative correlation with the period or gap distance, respectively.

As discussed by Liu *et al.* [65], the application conditions for EMT could be related to the quantity d/p , as these two parameters could effectively influence the cutoff wave vectors of surface modes or HMs. The EMT-application-region boundaries are estimated with a relative error of less than 10% (depicted as black dashed lines in Fig. 5). Specifically, it implies $d/p > 6.7$ or 26 for different or identical combinations of SiC/Ge multilayers, while for the [SiO₂/Ge] multilayers, the condition is $d/p > 12$ or 4, respectively. Moreover, the conclusion may not be applicable to II-II and IV-IV scenarios, because the Ge layers could reduce the coupling between typical ENZ modes, especially under extreme near-field conditions and indicate a different SPhP-resonance frequency; this has been theoretically discussed [66]. The application conditions for different multilayers underscore the significance of experimental verifications, as the coupling strengths of various modes could greatly vary from one species to another. These phenomena also coincide well with the previous results in Figs. 2–4.

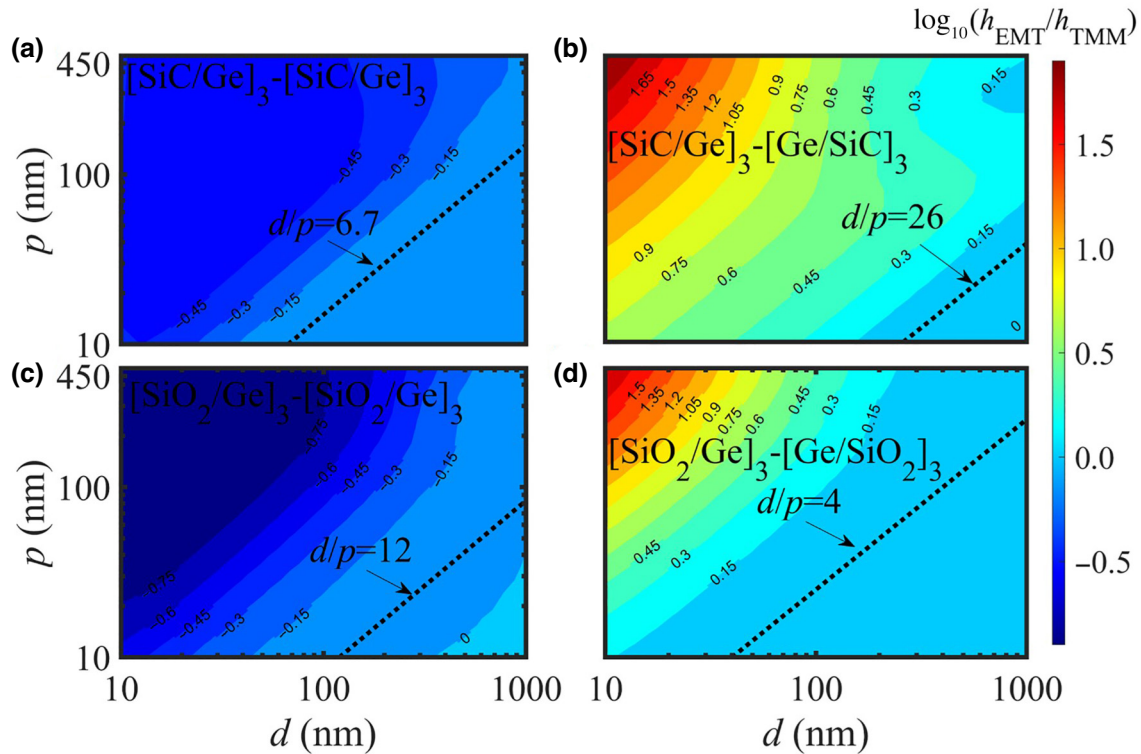


FIG. 5. Theoretical investigations of the relative error of EMT in predicting the NFRHT behaviors of (a),(b) [SiC/Ge]₃ and (c),(d) [SiO₂/Ge]₃ multilayers. (a),(c) Emitter and receiver combination with identical layer-stacking order, and (b),(d) with different layer-stacking order. Quantity d/p depicts the border of 10% deviation, as profiled by the black dashed lines.

V. CONCLUSION

From the infrared SiC/Ge and [SiO₂/Ge] multilayers fabricated in different stacking orders, the study of NFRHT (between these multilayers) reveals good agreement of the experimental results with the rigorous TMM predictions. Super-Planckian thermal radiation effects could be observed for samples with identical layer-stacking orders for the emitter and receiver. The experiment clearly indicates the failure of EMT at predicting the near-field heat flux, especially when there is strong surface-mode coupling, such as the ENZ mode. However, EMT can give a qualitative explanation of the energy-transmission process from the dispersion-band diagrams. In certain cases, such as the emitter and receiver combination of asymmetrical [SiO₂/Ge] stacking, EMT gives a good estimation of heat flux. Theoretical discussions on the applicability of EMT in NFRHT using the same configurations indicate that EMT's suitability depends on the ratio of the gap distance to structural period, which can vary significantly in terms of the multilayer constituents.

ACKNOWLEDGMENTS

The authors are grateful for partial support from NSFC (Grants No. 62075196 and No. 61775195); the NSFC of Zhejiang Province (Grants No. LXZ22F050001 and No. DT23F050006); and the Fundamental Research Funds for the Central Universities, the Leading Innovative and Entrepreneur Team Introduction Program of Zhejiang (Program No. 2021R01001). J.X. would like to thank the Research Grants Council of Hong Kong for support under Grant No. AoE/P-701/20.

APPENDIX: UNCERTAINTY ANALYSIS

The uncertainty in theoretical heat-flux predictions stems from various factors, including the bending of the chip, the roughness of the sample, nonuniformity in the height of the nanopillars, and nonuniformity in the thickness of multilayers. Measurements of bending (B_z) using a white-light interferometer (NewView 8200 Series, ZYGO, USA) revealed that the Si substrate exhibited superflat bending conditions, ranging from -15 to 15 nm, with some

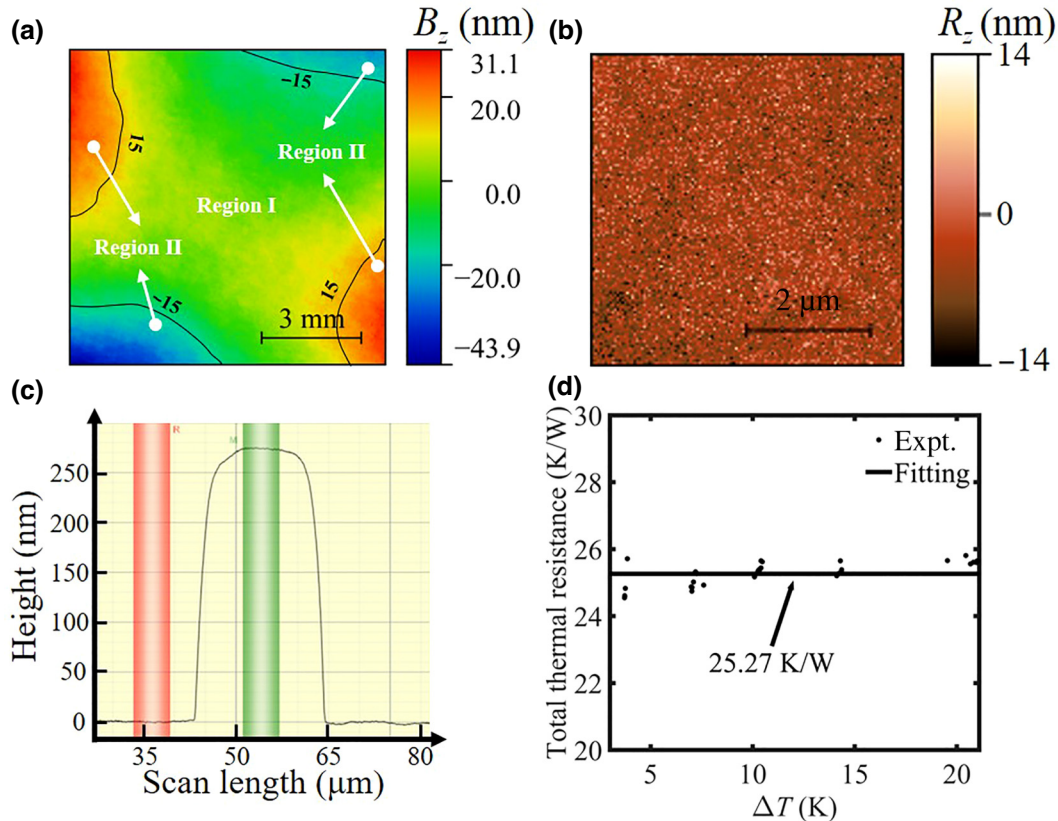


FIG. 6. (a) Bending morphology (B_z) of the substrate. Entire surface is divided into two regions by contour lines based on their level of bending, as marked by white arrows. (b) Roughness (R_z) of the multilayer sample. Measuring area is $5 \times 5 \mu\text{m}^2$. Average roughness, R_{av} , is 1.6 nm. (c) Morphology of SU-8 nanopillar. Height of nanopillar is estimated by the average value of vertical distance of red and green measuring bands. (d) Measured total thermal resistance of two adhesion layers of thermal conductive glue. Constant fitting of total thermal resistance is 25.27 K/W, as marked in the figure.

deviations at the four corners, as shown in Fig. 6(a). To more accurately assess the gap-distance uncertainty, the surface is divided into two regions: region I ($B_z = [-15, 15]$ nm, comprising 80% of the area) and region II ($B_z = [-43.9, -15]$ and $[15, 31.1]$ nm, comprising 20% of the area). These regions with different bending conditions may give rise to $[-30, 30]$ - and $[-62.2, 87.8]$ -nm gap uncertainties, respectively. The roughness (R_z) of the multilayer sample is evaluated using atomic force microscopy (Dimension Icon, Bruker, Germany), as shown in Fig. 6(b). The average roughness (R_{av}) is determined to be 1.6 nm, leading to a gap-distance uncertainty of $[-1.6, 1.6]$ nm. Additionally, the height of SU-8 photoresist nanopillars is measured to be 270 nm using a step profiler (Dektak 150, Veeco, USA), as depicted in Fig. 6(c). Accordingly, the impact of nonuniformity in height may introduce a gap uncertainty of $[-6, 6]$ nm. Moreover, the uncertainty of the multilayer thickness is determined from the SEM images in Fig. 1(c), resulting in thickness uncertainties of $[\text{SiC}(-1.7, 2.4) \text{ nm}]/\text{Ge}(-1.4, 2.7) \text{ nm}]_3$ and $[\text{SiO}_2(-4.3, 3.3) \text{ nm}]/\text{Ge}(-3.7, 2.4) \text{ nm}]_3$. These are also included in the uncertainty in theoretical heat-flux predictions, as the lower bound of the prediction area accounts for the thickest Ge layer and thinnest SiC/SiO₂ layer condition, while the upper bound represents the opposite scenario. Considering all the aforementioned uncertainties, predictions of TMM and EMT are accordingly calculated: 80% of the theoretical predictions are calculated with $270_{-37.6}^{+37.6}$ - nm gap distance and 20% are with $270_{-69.8}^{+95.4}$ - nm gap distance, as plotted in Fig. 2.

The uncertainties in experimental measurements arise from the uncertainties in temperature and heat-flux measurements. The temperature is measured by two thermistors at the heat spreaders of the emitter and receiver sides. However, the thermal resistance of adhesion layers could introduce extra temperature uncertainties. To mitigate this potential issue, as previously discussed [16], a calibration measurement for the thermal resistance of the adhesion layer (thermal conductive glue) is performed. Like the configuration in Fig. 1(b), we replace the multilayer samples with a single 500- μm -thick Si chip, which directly connects the up and down heat spreader with the same glue. Given the high thermal conductance of Si ($\sim 140 \text{ W/m}^2\text{K}$), the measured total thermal resistance is comprehensively determined by the combined resistance of the two adhesion layers:

$$R_{\text{total}} = 2R_{\text{glue}} = \frac{\Delta T}{QS}, \quad (\text{A1})$$

where ΔT is the temperature difference of the two heat spreaders, Q is the heat flux measured by HFS, and S is the surface area. As shown in Fig. 6(d), the measured R_{total} is 25.27 K/W, with a root-mean-square error (RMSE) of 0.366 K/W. This yields a thermal resistance of 12.64 K/W

for a single adhesion layer, which may lead to 1.2 K temperature deviation at a heat flux of 1000 W/m^2 , and is included in the plot of experimental data in Fig. 2. Regarding such a small RMSE of thermal resistance data, the uncertainty can be safely ignored. In this case, the temperature uncertainty is primarily influenced by the accuracy of the thermistor, which is $\pm 1 \text{ K}$, according to the supplier. Additionally, the uncertainty of measured heat flux is derived from the accuracy of the heat-flux sensor (3%), which is incorporated as the error bars in Fig. 2.

-
- [1] S. Basu, Z. M. Zhang, and C. J. Fu, Review of near-field thermal radiation and its application to energy conversion, *Int. J. Energy Res.* **33**, 1203 (2009).
 - [2] D. Polder and M. Van Hove, Theory of radiative heat transfer between closely spaced bodies, *Phys. Rev. B* **4**, 3303 (1971).
 - [3] R. Messina and M. Antezza, Scattering-matrix approach to Casimir-Lifshitz force and heat transfer out of thermal equilibrium between arbitrary bodies, *Phys. Rev. A* **84**, 042102 (2011).
 - [4] R. Messina and M. Antezza, Three-body radiative heat transfer and Casimir-Lifshitz force out of thermal equilibrium for arbitrary bodies, *Phys. Rev. A* **89**, 052104 (2014).
 - [5] A. W. Rodriguez, M. T. H. Reid, and S. G. Johnson, Fluctuating-surface-current formulation of radiative heat transfer: Theory and applications, *Phys. Rev. B* **88**, 054305 (2013).
 - [6] B. Liu, J. Li, and S. Shen, Resonant thermal infrared emitters in near- and far-fields, *ACS Photonics* **4**, 1552 (2017).
 - [7] J. Li, Z. Li, and S. Shen, Degenerate quasi-normal mode theory for near-field radiation between plasmonic structures, *Opt. Express* **28**, 34123 (2020).
 - [8] L. P. Walter, E. J. Tervo, and M. Francoeur, Near-field radiative heat transfer between irregularly shaped dielectric particles modeled with the discrete system Green's function method, *Phys. Rev. B* **106**, 195417 (2022).
 - [9] A. I. Volokitin, Effect of an electric field in the heat transfer between metals in the extreme near field, *JETP Lett.* **109**, 749 (2019).
 - [10] A. I. Volokitin, Electric double layer effect in an extreme near-field heat transfer between metal surfaces, *Phys. Rev. B* **103**, L041403 (2021).
 - [11] O. Vafek, Thermoplasma polariton within scaling theory of single-layer graphene, *Phys. Rev. Lett.* **97**, 266406 (2006).
 - [12] C.-L. Zhou, L. Qu, Y. Zhang, and H.-L. Yi, Enhancement and active mediation of near-field radiative heat transfer through multiple nonreciprocal graphene surface plasmons, *Phys. Rev. B* **102**, 245421 (2020).
 - [13] M. Lim, J. Song, S. S. Lee, and B. J. Lee, Tailoring near-field thermal radiation between metallo-dielectric multilayers using coupled surface plasmon polaritons, *Nat. Commun.* **9**, 4302 (2018).
 - [14] A. Ghanekar, L. Lin, J. Su, H. Sun, and Y. Zheng, Role of nanoparticles in wavelength selectivity of multilayered

- structures in the far-field and near-field regimes, *Opt. Express* **23**, A1129 (2015).
- [15] W. B. Zhang, C. Y. Zhao, and B. X. Wang, Enhancing near-field heat transfer between composite structures through strongly coupled surface modes, *Phys. Rev. B* **100**, 075425 (2019).
- [16] L. Tang, J. DeSutter, and M. Francoeur, Near-field radiative heat transfer between dissimilar materials mediated by coupled surface phonon- and plasmon-polaritons, *ACS Photonics* **7**, 1304 (2020).
- [17] G. T. Papadakis, B. Zhao, S. Buddhiraju, and S. Fan, Gate-tunable near-field heat transfer, *ACS Photonics* **6**, 709 (2019).
- [18] J. E. Pérez-Rodríguez, G. Pirruccio, and R. Esquivel-Sirvent, Spectral gaps in the near-field heat flux, *Phys. Rev. Mater.* **3**, 015201 (2019).
- [19] V. Fernandez-Hurtado, F. J. Garcia-Vidal, S. Fan, and J. C. Cuevas, Enhancing near-field radiative heat transfer with Si-based metasurfaces, *Phys. Rev. Lett.* **118**, 203901 (2017).
- [20] Y. Li, W. Li, T. Han, X. Zheng, J. Li, B. Li, S. Fan, and C.-W. Qiu, Transforming heat transfer with thermal metamaterials and devices, *Nat. Rev. Mater.* **6**, 488 (2021).
- [21] L. Xu and J. Huang, Metamaterials for manipulating thermal radiation: Transparency, cloak, and expander, *Phys. Rev. Appl.* **12**, 044048 (2019).
- [22] K. W. Lee, W. Lim, M. S. Jeon, H. Jang, J. Hwang, C. H. Lee, and D. R. Kim, Visibly clear radiative cooling metamaterials for enhanced thermal management in solar cells and windows, *Adv. Funct. Mater.* **32**, 2105882 (2022).
- [23] Q. Xu, X. Liu, Y. Xuan, Y. Xu, and D. Liu, High-performance infrared thermal radiation suppression metamaterials enabling inhibited infrared emittance and decreased temperature simultaneously, *Int. J. Heat Mass Transfer* **161**, 120318 (2020).
- [24] J. Shi, B. Liu, P. Li, L. Y. Ng, and S. Shen, Near-field energy extraction with hyperbolic metamaterials, *Nano Lett.* **15**, 1217 (2015).
- [25] W. Du, J. Yang, S. Zhang, N. Iqbal, Y. Dang, J.-B. Xu, and Y. Ma, Super-Planckian near-field heat transfer between hyperbolic metamaterials, *Nano Energy* **78**, 105264 (2020).
- [26] C. H. Lee and M. K. Seo, Broadband two-dimensional hyperbolic metasurface for on-chip photonic device applications, *Opt. Lett.* **45**, 2502 (2020).
- [27] X. Luo, H. Salihoglu, Z. Wang, Z. Li, H. H. Kim, J. Li, B. Yu, S. Du, and S. Shen, Nanodevice-enabled near-field thermal radiation between sub-wavelength surfaces, [arXiv:2308.13733](https://arxiv.org/abs/2308.13733) (2023).
- [28] L. Tang, L. i. M. Correa, M. Francoeur, and C. Dames, Large enhancement of near-field radiative heat transfer in the dual nanoscale regime enabled by electromagnetic corner and edge modes, [arXiv:2310.20356](https://arxiv.org/abs/2310.20356) (2023).
- [29] X. Liu and Z. Zhang, Near-field thermal radiation between metasurfaces, *ACS Photonics* **2**, 1320 (2015).
- [30] J. Dai, S. A. Dyakov, and M. Yan, Enhanced near-field radiative heat transfer between corrugated metal plates: Role of spoof surface plasmon polaritons, *Phys. Rev. B* **92**, 035419 (2015).
- [31] B. Liu and S. Shen, Broadband near-field radiative thermal emitter/absorber based on hyperbolic metamaterials: Direct numerical simulation by the Wiener chaos expansion method, *Phys. Rev. B* **87**, 115403 (2013).
- [32] K. Chen, B. Zhao, and S. Fan, MESH: A free electromagnetic solver for far-field and near-field radiative heat transfer for layered periodic structures, *Comput. Phys. Commun.* **231**, 163 (2018).
- [33] B. Liu, J. Shi, K. Liew, and S. Shen, Near-field radiative heat transfer for Si based metamaterials, *Opt. Commun.* **314**, 57 (2014).
- [34] M. Wang, L. Tang, C. Y. Ng, R. Messina, B. Guizal, J. A. Crosse, M. Antezza, C. T. Chan, and H. B. Chan, Strong geometry dependence of the Casimir force between interpenetrated rectangular gratings, *Nat. Commun.* **12**, 600 (2021).
- [35] C. R. Otey, L. Zhu, S. Sandhu, and S. Fan, Fluctuational electrodynamics calculations of near-field heat transfer in non-planar geometries: A brief overview, *J. Quant. Spectrosc. Radiat. Transfer* **132**, 3 (2014).
- [36] M. Liscidini, D. Gerace, L. C. Andreani, and J. E. Sipe, Scattering-matrix analysis of periodically patterned multilayers with asymmetric unit cells and birefringent media, *Phys. Rev. B* **77**, 035324 (2008).
- [37] R. Messina, A. Noto, B. Guizal, and M. Antezza, Radiative heat transfer between metallic gratings using Fourier modal method with adaptive spatial resolution, *Phys. Rev. B* **95**, 125404 (2017).
- [38] K. Park, S. Basu, W. P. King, and Z. M. Zhang, Performance analysis of near-field thermophotovoltaic devices considering absorption distribution, *J. Quant. Spectrosc. Radiat. Transfer* **109**, 305 (2008).
- [39] Y. Yang, J.-Y. Chang, P. Sabbaghi, and L. Wang, Performance analysis of a near-field thermophotovoltaic device with a metallodielectric selective emitter and electrical contacts for the photovoltaic cell, *J. Heat Transfer* **139**, 052701 (2017).
- [40] Y. Song, F. Jiang, N. Song, L. Shi, and P. Ding, Multilayered structural design of flexible films for smart thermal management, *Compos. Part A Appl. Sci. Manuf.* **141**, 106222 (2021).
- [41] H. Zhu, Q. Li, C. Zheng, Y. Hong, Z. Xu, H. Wang, W. Shen, S. Kaur, P. Ghosh, and M. Qiu, High-temperature infrared camouflage with efficient thermal management, *Light Sci. Appl.* **9**, 60 (2020).
- [42] B. Zhao, B. Guizal, Z. M. Zhang, S. Fan, and M. Antezza, Near-field heat transfer between graphene/hBN multilayers, *Phys. Rev. B* **95**, 245437 (2017).
- [43] J. Wu, F. Wu, T. Zhao, M. Antezza, and X. Wu, Dual-band nonreciprocal thermal radiation by coupling optical Tamm states in magnetophotonic multilayers, *Int. J. Therm. Sci.* **175**, 107457 (2022).
- [44] Y. Zhang, H.-L. Yi, H.-P. Tan, and M. Antezza, Giant resonant radiative heat transfer between nanoparticles, *Phys. Rev. B* **100**, 134305 (2019).
- [45] T. Wang, M. M. Sohoni, L. G. Wright, M. M. Stein, S.-Y. Ma, T. Onodera, M. G. Anderson, and P. L. McMahon, Image sensing with multilayer nonlinear optical neural networks, *Nat. Photonics* **17**, 408 (2023).
- [46] I. Latella, P. Ben-Abdallah, S.-A. Biehs, M. Antezza, and R. Messina, Radiative heat transfer and nonequilibrium

- Casimir-Lifshitz force in many-body systems with planar geometry, *Phys. Rev. B* **95**, 205404 (2017).
- [47] Y. Jeyar, K. Austray, M. Luo, B. Guizal, H. B. Chan, and M. Antezza, Casimir-Lifshitz force between graphene-based structures out of thermal equilibrium, *Phys. Rev. B* **108**, 115412 (2023).
- [48] C. Abbas, B. Guizal, and M. Antezza, Strong thermal and electrostatic manipulation of the Casimir force in graphene multilayers, *Phys. Rev. Lett.* **118**, 126101 (2017).
- [49] Y. Guo and Z. Jacob, Thermal hyperbolic metamaterials, *Opt. Express* **21**, 15014 (2013).
- [50] K. Ito, K. Nishikawa, A. Miura, H. Toshiyoshi, and H. Iizuka, Dynamic modulation of radiative heat transfer beyond the blackbody limit, *Nano Lett.* **17**, 4347 (2017).
- [51] C. Lucchesi, R. Vaillon, and P. O. Chapuis, Radiative heat transfer at the nanoscale: experimental trends and challenges, *Nanoscale Horiz.* **6**, 201 (2021).
- [52] N. Iqbal, S. Zhang, S. Wang, Z. Fang, Y. Hu, Y. Dang, M. Zhang, Y. Jin, J. Xu, B. Ju, and Y. Ma, Measuring near-field radiative heat transfer in a graphene-SiC heterostructure, *Phys. Rev. Appl.* **19**, 024019 (2023).
- [53] J. Yang, W. Du, Y. Su, Y. Fu, S. Gong, S. He, and Y. Ma, Observing of the super-Planckian near-field thermal radiation between graphene sheets, *Nat. Commun.* **9**, 4033 (2018).
- [54] T. Zhan, X. Shi, Y. Dai, X. Liu, and J. Zi, Transfer matrix method for optics in graphene layers, *J. Phys.: Condens. Matter* **25**, 215301 (2013).
- [55] O. Kidwai, S. V. Zhukovsky, and J. E. Sipe, Effective-medium approach to planar multilayer hyperbolic metamaterials: Strengths and limitations, *Phys. Rev. A* **85**, 053842 (2012).
- [56] A. Poddubny, I. Iorsh, P. Belov, and Y. Kivshar, Hyperbolic metamaterials, *Nat. Photonics* **7**, 948 (2013).
- [57] M. Tschikin, S.-A. Biehs, R. Messina, and P. Ben-Abdallah, On the limits of the effective description of hyperbolic materials in the presence of surface waves, *J. Opt.* **15**, 105101 (2013).
- [58] R. Kitamura, L. Pilon, and M. Jonasz, Optical constants of silica glass from extreme ultraviolet to far infrared at near room temperature, *Appl. Opt.* **46**, 8118 (2007).
- [59] Y. Guo, C. L. Cortes, S. Molesky, and Z. Jacob, Broadband super-Planckian thermal emission from hyperbolic metamaterials, *Appl. Phys. Lett.* **101**, 131106 (2012).
- [60] H. N. S. Krishnamoorthy, Z. Jacob, E. Narimanov, I. Kretzschmar, and V. M. Menon, Topological transitions in metamaterials, *Science* **336**, 205 (2012).
- [61] S. A. Biehs, M. Tschikin, and P. Ben-Abdallah, Hyperbolic metamaterials as an analog of a blackbody in the near field, *Phys. Rev. Lett.* **109**, 104301 (2012).
- [62] S. Vassant, J.-P. Hugonin, F. Marquier, and J.-J. Greffet, Berreman mode and epsilon near zero mode, *Opt. Express* **20**, 23971 (2012).
- [63] Y. Jin, S. Xiao, N. A. Mortensen, and S. He, Arbitrarily thin metamaterial structure for perfect absorption and giant magnification, *Opt. Express* **19**, 11114 (2011).
- [64] O. Ilic, M. Jablan, J. D. Joannopoulos, I. Celanovic, H. Buljan, and M. Soljačić, Near-field thermal radiation transfer controlled by plasmons in graphene, *Phys. Rev. B* **85**, 155422 (2012).
- [65] X. L. Liu, T. J. Bright, and Z. M. Zhang, Application conditions of effective medium theory in near-field radiative heat transfer between multilayered metamaterials, *J. Heat Transfer* **136**, 092703 (2014).
- [66] S.-A. Biehs and P. Ben-Abdallah, Near-field heat transfer between multilayer hyperbolic metamaterials, *Z. Naturforsch. A* **72**, 115 (2017).